Spatial Orientations of Hydraulically Conductive Shear Natural Fractures for an Arbitrary Stress State: an Analytical Study

Nikita Vladislavovich Dubinya[1]

[1]Moscow Institute of Physics and Technology

November 22, 2022

Abstract

The paper focuses on spatial orientations of hydraulically conductive shear fractures existing in naturally fractured fluid saturated rocks. Hydraulic conductivity of such fractures is considered from the current stress state of these rocks. The concept of critically stressed fractures is generally used to establish such relationship. The paper presents an analytical solution to the problem of obtaining all possible spatial orientations of critically stressed fractures for an arbitrary stress tensor. The proposed solution is explicit, providing an opportunity to predict the spatial orientations of hydraulically conductive fractures based on results of any sort of solutions to geomechanical problems considering naturally fractured rocks. The obtained results may be directly used for planning the development of oil fields, characterized by considerable contribution of fractures to permeability in cases when geomechanical modeling takes place. Several examples of applying the obtained solution in practice are presented in the paper: critically stressed fractures spatial orientations are considered for cases of gradual changes in stress tensor components under specific conditions providing an understanding of the main tendencies in these spatial orientations.

Spatial Orientations of Hydraulically Conductive Shear Natural Fractures for an Arbitrary Stress State: an Analytical Study

N. V. Dubinya[1,2]

[1] Moscow Institute of Physics and Technology, Russia, Dolgoprudny, Institutskiy per., 9, 141701.

[2] Schmidt Institute of Physics of the Earth of the Russian Academy of Sciences, Russia, Moscow, B. Gruzinskaya str., 10-1, 123242.

Corresponding author: Nikita Dubinya (Dubinya.NV@gmail.com)

Key Points:

- Hydraulic conductivity of natural fractures is related to current stress state
- Orientations of conductive fractures are obtained for an arbitrary stress tensor
- Various stress regimes are related to different patterns of conductive fractures.

14 **Abstract**

15 The paper focuses on spatial orientations of hydraulically conductive shear fractures existing in

16 naturally fractured fluid saturated rocks. Hydraulic conductivity of such fractures is considered

17 from the current stress state of these rocks. The concept of critically stressed fractures is

18 generally used to establish such relationship. The paper presents an analytical solution to the

19 problem of obtaining all possible spatial orientations of critically stressed fractures for an

20 arbitrary stress tensor. The proposed solution is explicit, providing an opportunity to predict the

21 spatial orientations of hydraulically conductive fractures based on results of any sort of solutions

22 to geomechanical problems considering naturally fractured rocks. The obtained results may be

23 directly used for planning the development of oil fields, characterized by considerable

24 contribution of fractures to permeability in cases when geomechanical modeling takes place.

25 Several examples of applying the obtained solution in practice are presented in the paper:

26 critically stressed fractures spatial orientations are considered for cases of gradual changes in

27 stress tensor components under specific conditions providing an understanding of the main

28 tendencies in these spatial orientations.

29 **Plain Language Summary**

30 Nowadays naturally fractured reservoirs are being developed in order to maintain and increase

31 the level of oil production. Natural fractures tend to provide the best paths for oil to flow, yet it is

32 a complicated problem to predict which fractures will provide such paths and which will not. It

33 appears that many factors influence these fractures including so-called geomechanical factors –

34 stresses and pressures acting at reservoir depth. While modern approaches make it possible to

35 predict the stress state of reservoirs, but relationship between stresses and oil filtration paths

36 remains a problem. The paper presents an analytical solution for spatial orientations of

37 hydraulically conductive natural fractures in an arbitrary stress state. This solution can find its

38 applications in a variety of areas in petroleum engineering including forecast of fractured zones

39 in reservoir, estimation of stress state of the upper layers of the Earth's crust based on well

40 logging data, hydrocarbon migration and others.

1 Introduction

The study is devoted to the problem of developing hydrocarbon reservoirs characterized by considerable contribution of natural fractures existing in fluid-saturated rock masses to their hydraulic properties. The main question of the paper is: how is it possible to use the existing approaches to reservoir behavior modeling in order to understand which reservoir zones are perspective for development due to existence of majority of natural hydraulically conductive fractures, and what are the preferable spatial orientations of these fractures? The latter point is extremely important for naturally fractured reservoir development as hydraulically conductive fractures provide filtration paths for fluid.

In the current study the stated question is answered from the point of view of geomechanical modeling. The approaches to three- and four-dimensional modeling of geomechanical processes taking place in the reservoirs (including fractured rocks) are now well-developed in the industry; there are algorithms for modeling the stress-strain state of a reservoir on different stages of development (Kolditz et al., 2016; Zhu et al., 2016).

There are a number of studies devoted to using the results of geomechanical modeling for analyzing the hydrodynamic properties of fractured rocks based on the concept of critically stressed fractures. This concept was proposed by Barton et al. (1995). According to the definition given in this paper, a fracture is considered to be critically stressed if shear stress acting on its surface is large enough for a slip to occur alongside the fracture's surface whenever differential stress is slightly increased. In order to determine whether a given fracture is critically stressed or not, one has to know the friction coefficient of the rock alongside with shear and normal stresses acting on its surface. These stresses, in turn, may be calculated if spatial orientation of the fracture and all components of the stress tensor in its vicinity are known. Barton et al. (1995) proved that critically stressed fractures are closely related to hydraulically conductive fractures by studying a well characterized by a high quality of well logs and existence of a reliable estimation of stress profiles. Classification of critically stressed and non-critically stressed fractures has been carried out revealing that the majority of critically stressed fractures tend to be hydraulically conductive as well. Hydraulic conductivity of particular fractures was estimated based on special well logs data. As a result, the following hypothesis was formulated: fractures which are critically stressed under current stress state tend to be hydraulically conductive and

71   non-critically stressed fractures tend to be non-hydraulically conductive. This hypothesis was

72   later proved to be valid for different hydrocarbon reservoirs (Hickman et al., 1997; Townend &

73   Zoback, 2000; Ito & Zoback, 2000; Rogers, 2003; Ligtenberg, 2005; Mattila & Follin, 2019) and

74   geothermal fields (Davatzes & Hickman, 2010; Davidson et al., 2012; Massiot et al., 2017).

75   This hypothesis was used as a basis for an algorithm of optimizing the well production.

76   One-dimensional geomechanical models are constructed on the basis of well logs data. These

77   models include stress profiles along the well trajectory, which are subsequently used to predict

78   zones containing critically stressed and, accordingly, hydraulically conductive fractures (Schwab

79   et al., 2017; Bayuk et al., 2019; Chan et al., 2019). It should be mentioned that the results of

80   detailed studies carried out in some regions (Fisher et al., 2003; Sathar et al., 2012; Bisdom et al.,

81   2016) prove that the hypothesis of a relationship between critically stressed and hydraulically

82   conductive fractures is not reliable in some cases. It is caused by geological factors, complex

83   history of stress-strain state evolution in the region, and nonlinear rheological effects not taken

84   into account in critically stressed fractures concept.

85   The concept of critically stressed fractures is also used for solving the inverse problem of

86   stress estimation based on geophysical data for solving the important problems of wellbore

87   stability (Ito et al., 2002; Dubinya & Ezhov, 2017; Dubinya, 2019). In this case the inverse

88   problem is formulated as follows: one needs to reconstruct the stress profiles along the trajectory

89   of a certain well based on the given information on which natural shear fractures in its vicinity

90   are critically stressed, and which ones are not. The following algorithm is generally used in these

91   studies mainly devoted to reconstruct stress profiles along the well trajectory. On the first step

92   data obtained from special well logging techniques are used for determination of spatial

93   orientations of all natural shear fractures observed in the well vicinity (Silva et al., 2003). Then

94   estimations of some properties of well surrounding rock mass (temperature profiles (Ito et al.,

95   2002), resistivity and acoustic properties distributions (Dubinya & Ezhov, 2017), or elastic

96   moduli profiles (Dubinya, 2019)) are used to classify fractures as critically stressed or non-

97   critically stressed. Finally, the profiles of principal stresses are adjusted in a way to obtain the

98   best match between critically stressed fractures classification based on well logs, and the same

99   classification based on stress profiles.

100   To sum up, critically stressed fractures concept is generally used in different areas of

101 hydrocarbon reservoir geomechanics in cases of naturally fractured rock. The strong relationship

102 between critically stressed and hydraulically conductive fractures increases the value of

103 geomechanical modeling results as they give certain assumptions on fluid filtration.

104   The current paper presents a mathematical algorithm for direct calculation of all the

105 possible spatial orientations of critically stressed fractures for an arbitrary given stress tensor. As

106 far as an arbitrary stress tensor is considered, the hypothesis of one principal axis of stress tensor

107 being subvertical, which is often used in problems of reservoir geomechanics (Zoback, 2007),

108 may be avoided. It broadens the opportunities of critically stressed fractures analysis for solving

109 the problems of fractured reservoirs development. The solution can find its applications in a

110 variety of areas in petroleum engineering including forecast of fractured zones in reservoir,

111 estimation of stress state of the upper layers of the Earth's crust based on well logging data,

112 hydrocarbon migration and others.

2 Theory

114   According to initial definition given by Barton et al. (1995) a fracture is referred to as

115 critically stressed, if normal and shear stresses acting on its surface satisfy the raw friction

116 criterion:

117 $$\tau_n \geq \mu \cdot \sigma_n. \tag{1}$$

118   Here τ_n is shear stress acting on the fracture plane; σ_n is normal stress acting on the

119 fracture plane; μ is friction coefficient of the rock mass. The value of friction coefficient μ is

120 often defined as 0.6 following the well-known experiments (Byerlee, 1978) yet it is necessary to

121 carry out special experiments to precisely estimate it for the specific rock. This coefficient is not

122 specified for the analytical solution of the critically stressed fractures spatial orientations

123 problem. In the most sections of this paper μ will be 0.6 as well.

124   Let's consider a volume of rock mass containing a number of microcracks. This c volume

125 is characterized by an arbitrary stress tensor σ_{ij} with its principal components denoted as σ_1, σ_2,

126 and σ_3. The following notation is used hereafter: compression is regarded as positive and $\sigma_1 \geq \sigma_2$

127 $\geq \sigma_3$. As fluid-saturated rock masses are studied in the paper, all the stresses will be considered as

128 effective in terms of theory of poroelasticity (Biot, 1955; Coussy, 2004). All fractures and

129   microcracks will be considered as planes and their spatial orientations will be described using the

130   vectors normal to these planes or normal vectors.

131   In this paper critically stressed fractures will be often analyzed with the usage of Mohr's

132   diagram (Fig. 1) where axes represent the magnitudes of normal and shear stresses acting on any

133   plane. The given values of principal stresses σ_1, σ_2, and σ_3 make it possible to construct Mohr's

134   circle shown as a solid black line in Fig. 1. It can be shown that a dot representing any fracture

135   existing in the given stress state (with fixed principal stresses) is to stay inside the area bordered
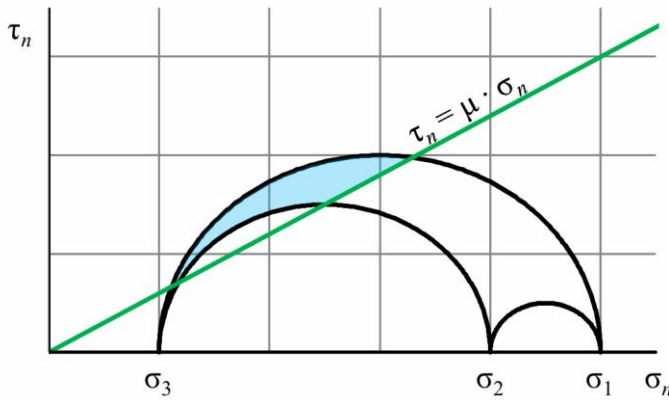
136   by Mohr's circle.

138   **Figure 1.** Schematic representation of critically stressed fractures at Mohr's diagram.

139   Raw friction law (1) is represented by solid green line in Fig. 1. Respectively, dots,

140   representing all the fractures with criterion (1) being satisfied, are to be above the green line. As

141   a result, dots representing critically stressed fractures are to stay inside a limited domain shown

142   in blue in Fig. 1.

143   In order to calculate normal and shear stresses acting on a plane with a given spatial

144   orientation one has to know the full stress tensor acting in the elementary volume containing this

145   plane. Normal and shear stresses may be calculated as:

$$\sigma_n = \sigma_2 + l^2(\sigma_1 - \sigma_2) + n^2(\sigma_3 - \sigma_2), \tag{2}$$

$$\tau_n^{\ 2} = \left(\frac{\sigma_2 - \sigma_3}{2}\right)^2 + l^2(\sigma_1 - \sigma_2)(\sigma_1 - \sigma_3) - \left(\sigma_n - \frac{\sigma_2 + \sigma_3}{2}\right)^2, \tag{3}$$

148   where l is the cosine of an angle between normal vector to a considered plane and

149   direction of maximum principal stress σ_1; n is the cosine of an angle between normal vector to a

150   considered plane and direction of minimum principal stress σ_1. l and n will be referred to as

151   direction cosines of a normal vector to a fracture's plane or simply direction cosines hereafter.

152   The pair of normal and shear stresses provide coordinates to the dot representing a fracture on

153   Mohr's diagram. It should be noted, that normalized Mohr's diagram may be used for analysis as

154   principal stresses are linearly included into equations (2) and (3).

155   The following problem may be solved. For the given principal stresses magnitudes σ_1, σ_2,

156   and σ_3 one needs to find the variety of direction cosines l and n providing normal σ_n and shear τ_n

157   stresses satisfying criterion (1). Equations (2) and (3) defining a dot on Mohr's diagram are

158   equivalent to a system of two equations:

159
$$\tau_n^2 + \left(\sigma_n - \frac{\sigma_2 + \sigma_3}{2} \right)^2 = \left(\frac{\sigma_2 - \sigma_3}{2} \right)^2 + l^2 (\sigma_1 - \sigma_2)(\sigma_1 - \sigma_3), \tag{4}$$

160
$$\tau_n^2 + \left(\sigma_n - \frac{\sigma_1 + \sigma_2}{2} \right)^2 = \left(\frac{\sigma_1 - \sigma_2}{2} \right)^2 + n^2 (\sigma_3 - \sigma_1)(\sigma_3 - \sigma_2). \tag{5}$$

161   These equations have a geometrical meaning of the intersection point of two circles with

162   centers having coordinates (0; $(\sigma_1 + \sigma_2)/2$) and (0; $(\sigma_2 + \sigma_3)/2$), and radii $(\sigma_1 - \sigma_2)^2/4 + n^2(\sigma_3 -$

163    $\sigma_1)(\sigma_3 - \sigma_2)$ and $(\sigma_2 - \sigma_3)^2/4 + l^2(\sigma_1 - \sigma_2)(\sigma_1 - \sigma_3)$. Zero values of l and n are related to two small

164   Mohr's circles themselves; gradual increase of these cosines provides an increase in circles'

165   radii.

166   If a gradual increase of direction cosine n is considered, the first critically stressed

167   fracture will emerge at the moment of the first intersection between circle (5) and the raw friction

168   law line $\tau_n = \mu \cdot \sigma_n$. The corresponding value of direction cosine n is:

169
$$n_A = \sqrt{\frac{\tau_n^{A2} + \left(\sigma_n^A - \frac{\sigma_1 + \sigma_2}{2} \right)^2 - \left(\frac{\sigma_1 - \sigma_2}{2} \right)^2}{(\sigma_3 - \sigma_1)(\sigma_3 - \sigma_2)}}, \tag{6a}$$

170
$$\sigma_n^A = \frac{\sigma_1 + \sigma_2}{2(\mu^2 + 1)}, \tag{6b}$$

171
$$\tau_n^A = \mu \cdot \sigma_n^A. \tag{6c}$$

172   The upper index A in these sequation represents the name of the point of intersection

173   between circle (5) with radius (6a) and raw friction law.

174   It should be noted that technically this point may lie outside the area bordered by Mohr's

175   circle preventing these stresses to be realized on the plane of any fracture. That means that the

176   values of direction cosine n are also determined by intersections between the outer Mohr's circle

177   and raw friction law. Let the outer Mohr's circle intersect the raw friction law at points B and C

178   with point C staying to the right (Fig. 2a and 2b). Point A with coordinates calculated from

179   equation (6) is given on these figures as well.

180   The values of normal and shear stress at points B and C and the corresponding value of

181   direction cosine n are equal to:

182   For point B:

183
$$n_B = \sqrt{\frac{\tau_n^{B2} + \left(\sigma_n^B - \dfrac{\sigma_1 + \sigma_2}{2}\right)^2 - \left(\dfrac{\sigma_1 - \sigma_2}{2}\right)^2}{(\sigma_3 - \sigma_1)(\sigma_3 - \sigma_2)}},$$
(7a)

184
$$\sigma_n^B = \frac{\sigma_1 + \sigma_3 - \sqrt{(\sigma_1 + \sigma_3)^2 - 4\sigma_1\sigma_3(\mu^2 + 1)}}{2(\mu^2 + 1)},$$
(7b)

185
$$\tau_n^B = \mu \cdot \sigma_n^B.$$
(7c)

186

187   For point C:

188
$$n_C = \sqrt{\frac{\tau_n^{C2} + \left(\sigma_n^C - \dfrac{\sigma_1 + \sigma_2}{2}\right)^2 - \left(\dfrac{\sigma_1 - \sigma_2}{2}\right)^2}{(\sigma_3 - \sigma_1)(\sigma_3 - \sigma_2)}},$$
(8a)

189
$$\sigma_n^C = \frac{\sigma_1 + \sigma_3 + \sqrt{(\sigma_1 + \sigma_3)^2 - 4\sigma_1\sigma_3(\mu^2 + 1)}}{2(\mu^2 + 1)},$$
(8b)

190
$$\tau_n^C = \mu \cdot \sigma_n^C.$$
(8c)

191   That means that the values of direction cosine n for critically stressed fractures are to stay

192   inside the following limits:

193
$$n \in \left[\max(n_A; n_C);\quad n_B\right],$$
(9)

194   where the values of n_A, n_B, and n_C are calculated from equations (6) through (8).

195   Figures 2a and 2b represent the discussed points for a certain stress state with fixed

196   principal stresses. Fig. 2a is plotted for the case of $n_A < n_C$, and Fig. 2b represents the case $n_A >$

197   n_C. Equation (9) presents all the possible values of one direction cosine for fractures being

198   critically stressed under principal stresses σ_1, σ_2, and σ_3. Note that direction cosines appearing in

199   these equations are calculated for a coordinate system associated with principal axes of stress

200   tensor.

201   In order to solve the stated problem one needs to determine the interval of possible values

202   of direction cosine l standing for critically stressed fractures for every value of n inside the

203   interval (9). It is possible to determine the coordinates of points of intersection between circle (5)

204   and raw friction law line for any value of direction cosine n from the obtained interval. These

205   points are represented as D and E (E is to the right of D on Mohr's diagram, or $\sigma_n^E > \sigma_n^D$, Figures

206   2c and 2d), and their coordinates are:

207   For point D:

208
$$\sigma_n^D = \frac{-b - \sqrt{b^2 - 4c}}{2}, \tag{10a}$$

209
$$\tau_n^D = \mu \cdot \sigma_n^D, \tag{10b}$$

210
$$b = -\frac{\sigma_1 + \sigma_2}{\mu^2 + 1}, \tag{10c}$$

211
$$c = -\frac{n^2(\sigma_3 - \sigma_1)(\sigma_3 - \sigma_2) - \sigma_1\sigma_2}{\mu^2 + 1}. \tag{10d}$$

212   For point E:

213
$$\sigma_n^E = \frac{-b + \sqrt{b^2 - 4c}}{2}, \tag{11a}$$

214
$$\tau_n^E = \mu \cdot \sigma_n^E, \tag{11b}$$

215
$$b = -\frac{\sigma_1 + \sigma_2}{\mu^2 + 1}, \tag{11c}$$

216
$$c = -\frac{n^2(\sigma_3 - \sigma_1)(\sigma_3 - \sigma_2) - \sigma_1\sigma_2}{\mu^2 + 1}, \tag{11d}$$

217   If these values are introduced into equation (4), the following corresponding values of

218   direction cosine l are obtained:

219
$$l_D = \sqrt{\frac{\tau_n^{D2} + \left(\sigma_n^D - \frac{\sigma_2 + \sigma_3}{2}\right)^2 - \left(\frac{\sigma_2 - \sigma_3}{2}\right)^2}{(\sigma_1 - \sigma_2)(\sigma_1 - \sigma_3)}}, \tag{12a}$$

220
$$l_E = \sqrt{\frac{\tau_n^{E2} + \left(\sigma_n^E - \frac{\sigma_2 + \sigma_3}{2}\right)^2 - \left(\frac{\sigma_2 - \sigma_3}{2}\right)^2}{(\sigma_1 - \sigma_2)(\sigma_1 - \sigma_3)}}. \tag{12b}$$

221   In the same way as before, point E (which is to the right of point D) may geometrically

222   stay outside the area bordered by Mohr's circle. As a result, the corresponding stresses cannot be

223   realized. In order to take into account this opportunity, one has to consider point F – the point of

224   intersection between circle (5) and the outer Mohr's circle – and calculate its coordinates and

225   corresponding value of direction cosine l:

226
$$l_F = \sqrt{\frac{\tau_n^{F2} + \left(\sigma_n^F - \frac{\sigma_2 + \sigma_3}{2}\right)^2 - \left(\frac{\sigma_2 - \sigma_3}{2}\right)^2}{(\sigma_1 - \sigma_2)(\sigma_1 - \sigma_3)}}, \tag{13a}$$

227
$$\sigma_n^F = \sigma_1 + n^2(\sigma_3 - \sigma_1), \tag{13b}$$

228
$$\tau_n^F = \sqrt{\left(\frac{\sigma_1 - \sigma_3}{2}\right)^2 - \left(\sigma_n^F - \frac{\sigma_1 + \sigma_3}{2}\right)^2}. \tag{13c}$$

229   As a result, for any value of n chosen from the interval (9), one may calculate the interval

230   of the second direction cosine l values to satisfy the critically stressed fractures criterion (1). This

231   interval is dependent on n and has the following form:

232
$$l \in \left[l_D(n); \quad \min\left(l_E(n); l_F(n)\right)\right]. \tag{14}$$

233   If one needs to obtain the possible values of the third direction cosine m (cosine of angle

234   between normal vector to a fracture plane and direction of intermediate principal stress σ_2) of

235   critically stressed fractures, usual normalization should be used (l and n are taken from intervals

236   (9) and (14)):

237
$$m = \sqrt{1 - l^2 - n^2}. \tag{15}$$

238   Fig. 2 schematically represents the Mohr's diagrams, Mohr's circles, raw friction law,

239   and points A, B, C, D, E, and F with the same notation as above.
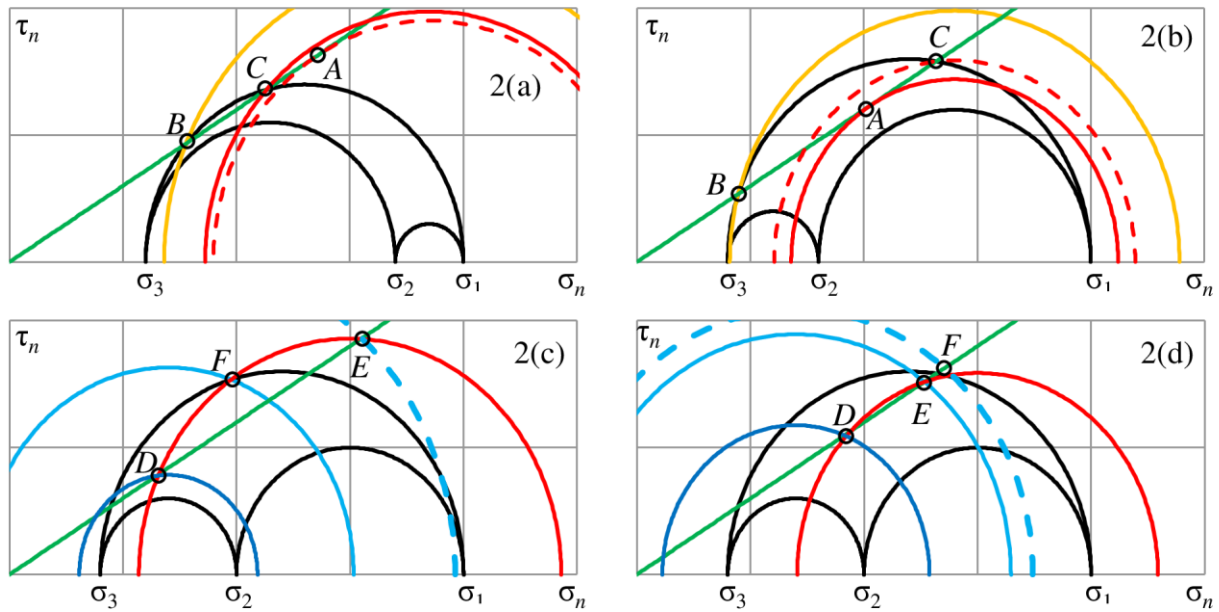

Figure 2. Schematic representation of the Mohr's circles used for theoretical solution.

242   Figures 2a and 2b are related to equations (6) through (9). Red line represents the circle

243   (5) corresponding to the minimum value of direction cosine n from the interval (9); yellow color

244   represents the maximum value of the same interval. Fig. 2a represents the case of $n_A < n_C$, the

245   circle related to n_A value is plotted as dotted line. In the corresponding way, Fig. 2b represents

246   the situation of $n_A > n_C$, with n_C-related circle plotted as dotted line. Figures 2c and 2d are related

247   to equations (10) through (14). At these plots one n value is chosen from the interval (9), and red

248   line is related to circle (5). Blue lines represent the circles (4) with the boundary values of l from

249   the interval (14). Dark blue line represents the minimum l value, and light blue line stands for the

250   maximum value. Two cases are considered in the same way as before $l_E > l_F$ (Fig. 2c) and $l_E < l_F$

251   (Fig. 2d). Dotted circle is related to the maximum of these two values.

252   As a result, the algorithm for finding all possible combinations of direction cosines l and

253   n for given principal stresses σ_1, σ_2, and σ_3 is established. First of all, the coordinates of the

254   critical points A, B, and C and corresponding values of direction cosines n_A, n_B, and n_C are

255   calculated according to equations (6) through (8). The interval of possible values of n is

256   determined as (9). Then for each value of n inside the calculated interval the coordinates of

257   critical points D, E, and F and corresponding values of direction cosines l_D, l_E, and l_F are

258   determined according to equations (10) through (13). Finally, for each value of n from the

259   interval (9) the interval of corresponding direction cosines l is calculated following equation

260   (14). Each pair of direction cosines l and n is combined with the third cosine m obtained from

261   equation (15). As a result, the magnitudes of principal stresses and friction coefficient μ give a

262   certain variety of combinations l, m, and n defining spatial orientations of vectors $\mathbf{n}$ normal to all

263   critically stressed fractures:

264
$$\mathbf{n} = \begin{pmatrix} l \in \left[l_D(n); \quad \min\left(l_E(n); l_F(n)\right) \right] \\ m = \sqrt{1 - l^2 - n^2} \\ n \in \left[\max\left(n_A; n_C\right); \quad n_B \right] \end{pmatrix}, \tag{16}$$

265   Coordinates of the normal vector $\mathbf{n}$ are given here for a coordinate system related to

266   principal axes of the considered stress tensor.

267   Despite the study of critically stressed fractures being relatively easy with Mohr's

268   diagram, real data on fractures are typically analyzed using angles, characterizing the fractures'

269   spatial orientations in a certain geographical coordinate system regardless of principal stresses

270   directions and normal vectors to fractures' planes. Such angles include strike and dip angles for

271   example. In order to turn direction cosines into these angles one has to carry out several

272   operations.

273   Consider a coordinate system with the first axis directed at gravitational force direction,

274   the second axis directed to the East and the third – to the North. An arbitrary stress tensor σ_{ij} is

275   considered in this coordinate system with its components being equal to:

276
$$\sigma_{ij} = \begin{bmatrix} \sigma_{11} & \sigma_{12} & \sigma_{13} \\ \sigma_{21} & \sigma_{22} & \sigma_{23} \\ \sigma_{31} & \sigma_{32} & \sigma_{33} \end{bmatrix}, \tag{15}$$

277   The principal values of this positive definite symmetric tensor are determined from

278   characteristic equation (λ are the eigenvalues of (15)):

279
$$\det(\sigma_{ij} - \lambda\delta_{ij}) = 0, \tag{16}$$

280   where δ_{ij} is Kronecker delta, $i, j = 1, 2, 3$. This equation has three roots σ_1, σ_2, and σ_3,

281   which are the principal stresses used above. Directions of these principal stresses are determined

282   from system of the equations:

283

$$\begin{cases} \left(\sigma_{11} - \sigma_k\right) n_1^{\ k} + \sigma_{12} n_2^{\ k} + \sigma_{13} n_3^{\ k} = 0, \\ \sigma_{21} n_1^{\ k} + \left(\sigma_{22} - \sigma_k\right) n_2^{\ k} + \sigma_{23} n_3^{\ k} = 0, \\ \sigma_{31} n_1^{\ k} + \sigma_{32} n_2^{\ k} + \left(\sigma_{33} - \sigma_k\right) n_3^{\ k} = 0, \\ \left(n_1^{\ k}\right)^2 + \left(n_2^{\ k}\right)^2 + \left(n_3^{\ k}\right)^2 = 1. \end{cases} \tag{17}$$

284   Here $k = 1, 2, 3$; $n_p^{\ k}$ is the cosine of an angle between direction of principal stress σ_k and

285   coordinate system axis numbered p ($p = 1, 2, 3$).

286   As a result, normal vectors **n** to critically stressed fractures planes will have the following

287   coordinates in a global coordinate system:

288

$$\begin{pmatrix} l_0 \\ m_0 \\ n_0 \end{pmatrix} = \begin{pmatrix} n_1^1 & n_1^2 & n_1^3 \\ n_2^1 & n_2^2 & n_2^3 \\ n_3^1 & n_3^2 & n_3^3 \end{pmatrix} \cdot \begin{pmatrix} l \in \left[l_D(n); \quad \min\left(l_E(n); l_F(n)\right) \right] \\ m = \sqrt{1 - l^2 - n^2} \\ n \in \left[\max\left(n_A; n_C\right); \quad n_B \right] \end{pmatrix}, \tag{18}$$

289   where $n_p^{\ k}$ are obtained from equations (17). l_0, m_0, and n_0 are the resultant direction

290   cosines of critically stressed fractures in the introduced global coordinate system. Once the

291   values of n_A, n_B, n_C, $l_D(n)$, $l_E(n)$, and $l_F(n)$ are calculated from principal stresses via equations (6)

292   through (8) and (10) through (13), the posed problem is solved: spatial orientations of critically

293   stressed fractures are obtained for an arbitrary stress tensor σ_{ij} (15). Although it generally solves

294   the posed problem, some further considerations are to be carried out to simplify the further usage

295   of the obtained solution.

296   Lambert azimuthal equal-area projection (a detailed description of using this projection to

297   analyze strike and dip angles is given by Snyder (1987) and Allmendinger et al. (2012)) will be

298   used in the current study to interpret the direction cosines in terms of structural geology. The

299   following approach is used to show principal stresses' directions on lower hemisphere Lambert

300   equal area stereonet. A sphere of unit radius is constructed from the center of coordinate system;

301   latitude and longitude of the point of intersection between this sphere and vector in direction of

302   the considered principal stress are calculated. For the coordinate system used in this study

303   latitude φ_k and longitude λ_k of direction of principal stress σ_k are calculated as:

304
$$\varphi_k = \arctan\left(\frac{n_3^{\,k}}{\sqrt{\left(n_1^{\,k}\right)^2 + \left(n_2^{\,k}\right)^2}}\right), \tag{19a}$$

305
$$\lambda_k = \arctan\left(\frac{n_2^{\,k}}{n_1^{\,k}}\right). \tag{19b}$$

306   Each three cosines l_0, m_0, and n_0 of critically stressed fractures are interpreted as

307   longitude and latitude in a way analogous to principal stresses' directions (19) as:

308
$$\varphi = \arctan\left(\frac{n_0}{\sqrt{\left(l_0\right)^2 + \left(m_0\right)^2}}\right), \tag{20a}$$

309
$$\lambda_k = \arctan\left(\frac{m_0}{l_0}\right). \tag{20b}$$

310   As far as equation (18) presents a variety of direction cosines of normal vectors to

311   critically stressed fractures planes, equations (20) give a domain of critically stressed fractures on

312   a stereonet contrary to equations (19) which give nothing more than three dots on the stereonet

313   corresponding to each of the principal stresses.

314   The overall procedure of obtaining spatial orientations of critically stressed fractures for a

315   given stress tensor σ_{ij} may be formulated as follows: **I.** Calculation of principal stress magnitudes

316   and directions by finding eigenvectors of tensor σ_{ij}. **II.** Calculation of limits on spatial orientation

317   of critically stressed fractures in principal stresses space using equations (6) through (16). **III.**

318   Calculation of direction cosines of the poles to critically stressed fractures planes in a global

319   coordinate system using equation (18). **IV.** Visual representation of the obtained results at

320   stereonet with the help of equations (19) and (20). It seems important to notice that the

321   mentioned procedure may be completed for any arbitrary stress tensor σ_{ij} without any

322   assumptions regarding its direct form (except its symmetry which is typical for the majority of

323   geomechanical problems).

324   An example of plotted directions of principal stresses corresponding to stress tensor with

325   components $\sigma_{11} = 25$ MPa, $\sigma_{22} = 18$ MPa, $\sigma_{33} = 8$ MPa, $\sigma_{12} = \sigma_{21} = -7$ MPa, $\sigma_{13} = \sigma_{31} = 1$ MPa,

326    $\sigma_{23} = \sigma_{32} = -3$ MPa on lower hemisphere Lambert equal area stereonet is shown in Fig. 3a

327   alongside with the corresponding domains of critically stressed fractures. The following

328   nomenclature will be used hereafter to plot the stereonets: maximum compressive stress σ_1 will

329   be represented by a red dot; intermediate principal compressive stress σ_2 – by a yellow dot; least

330   principal compressive stress σ_3 – by a green dot. Tensile stresses will not be considered. Solid

331   lines (blue in this current case) will serve as boundaries for the domains of critically stressed

332   fractures. Domain of critically stressed fractures is filled with blue in this figure showing the

333   typical area bordered by solid lines – it will not be filled in the subsequent figures. Fig. 3b

334   represents the possible values of direction cosines l and n calculated from equations (6) through

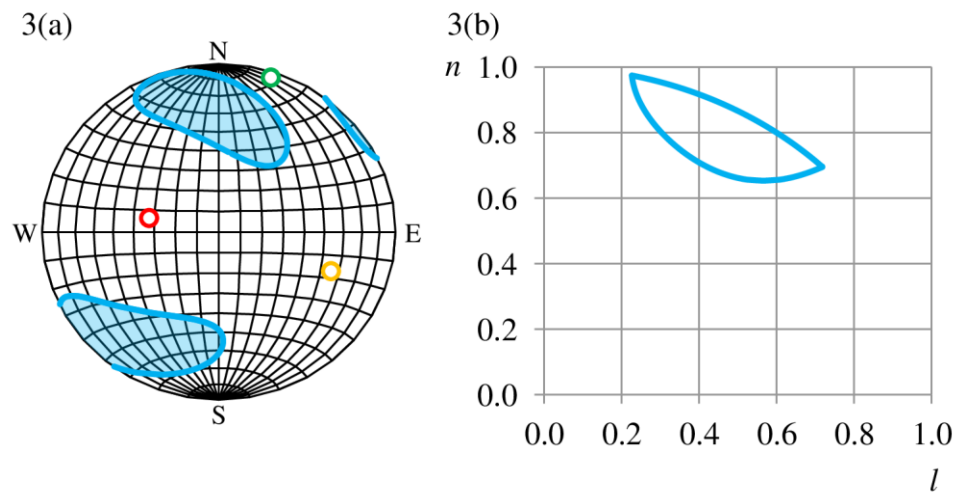335   (16) for the considered stress tensor.

336

337   **Figure 3.** An example of positioning critically stressed fractures at stereonet and

338   direction cosines diagram.

339   The given example is of illustrative nature. It shows that it is enough to know friction

340   coefficient to determine all possible spatial orientations of fractures being critically stressed in a

341   given stress state characterized by an arbitrary stress tensor σ_{ij}. Despite some difficulties

342   emerging during mathematical description of critically stressed fractures' spatial orientations, the

343   developed algorithm may be applied to the results of geomechanical modeling containing

344   distributions of stress tensor components. It is to be mentioned that all provided equations

345   dealing with stresses are relevant to effective stresses following Biot's theory.

346   The obtained solution presents an opportunity to qualitatively estimate the relative

347   amount of critically stressed fractures. Dubinya and Fokin (2018) proposed the coefficient S_{crit}

348   connected to relative amount of critically stressed fractures as the ratio between the area of

349   domain of critically stressed fractures above the raw friction line at Mohr's diagram (Fig. 1) and

350   the whole area of Mohr's circle. It was discussed that this ratio is equal to the relative amount of

351   critically stressed fractures for a representative volume of an "ideal" rock characterized by

352   uniform distribution of spatial cosines l and n of natural shear fractures. Although this value

353   can't be directly considered as fraction of critically stressed fractures in rock because uniform

354   distribution of natural fractures orientations is not typical for real rocks, it is possible to consider

355   this value as a qualitative measure of the relative amount of critically stressed fractures. The

356   explicit equations for relative amount of critically stressed fractures S_{crit} are:

357
$$S_{crit} = \frac{8\left(S_{13} - S_{12} - S_{23}\right)}{\pi\left(\left(\sigma_1 - \sigma_3\right)^2 - \left(\sigma_1 - \sigma_2\right)^2 - \left(\sigma_2 - \sigma_3\right)^2\right)},$$
(21a)

358   where S_{ij} $(i, j = 1, 2, 3)$ are non-zero in case of positive value of $(\sigma_i + \sigma_j)^2 - 4(\mu^2 + 1)$ and

359   are equal to:

360
$$S_{ij} = \frac{(\sigma_i - \sigma_j)^2}{8}\left(\begin{array}{c} \arccos B_{ij} - \arccos A_{ij} + \\ + B_{ij}\sqrt{1 - A_{ij}^2} - A_{ij}\sqrt{1 - B_{ij}^2} \end{array}\right),$$
(21b)

361   where

362
$$A_{ij} = \frac{-\mu^2(\sigma_i + \sigma_j) + \sqrt{(\sigma_i + \sigma_j)^2 - 4(1 + \mu^2)\sigma_i\sigma_j}}{(1 + \mu^2)(\sigma_i - \sigma_j)},$$
(21c)

363
$$B_{ij} = \frac{-\mu^2(\sigma_i + \sigma_j) - \sqrt{(\sigma_i + \sigma_j)^2 - 4(1 + \mu^2)\sigma_i\sigma_j}}{(1 + \mu^2)(\sigma_i - \sigma_j)}.$$
(21d)

364   As a result, any naturally fractured rock subjected to stresses (15) may be characterized

365   by spatial orientations of fractures that are critically stressed under the given conditions

366   (equations (6) through (18)) and their relative amount obtained from equations (21), which

367   concludes the section devoted to analytical solution of critically stressed fractures spatial

368   orientations problem.

369   The following sections present some applications of the obtained solution to consider the

370   typical tendencies in critically stressed fractures spatial orientations for variations of stress tensor

371   components.

3 Illustrative examples

373   The evolution of stereonets representing critically stressed fractures spatial orientations

374   and their relative amount is considered for cases of gradual changes of various parameters of

375   stress tensor (15) or rock properties in this section.

3.1 Principal axes rotation

377   It is convenient to start analysis of different stress tensors and corresponding critically

378   stressed fractures spatial orientations from the rotation of principal axes of the stress tensor.

379   It is typical for reservoir geomechanics problems (Zoback, 2007) to consider stress tensor

380   (15) in accordance with well-known Anderson's classification of stress regimes (Anderson,

381   1951) and new fault types: new formed faults will be normal, strike-slip, or reverse depending on

382   whether the maximum σ_1, intermediate σ_2, or minimum compressive stress σ_3 is directed

383   vertically. These types have been extended to include transitional cases (Philip, 1987; Guiraud et

384   al., 1989) between stress regimes caused by gradual increases in certain components of stress

385   tensor. These transitions may be quantitatively analyzed with introduction of specific tensor

386   shape parameters summarized by Célérier (1995). In the current study the convenient form of

387   generalized stress tensor shape parameter proposed by Simpson (1997) will be used to analyze

388   various stress states from the perspective of critically stressed fractures.

389   Fig. 4 gives a schematic representation of three Anderson's stress regimes: Normal Fault

390   (σ_1 is directed vertically), Strike-Slip (σ_2 is directed vertically), and Reverse Fault (σ_3 is directed

391   vertically). These three cases are typical for upper layers of the Earth's crust, but, generally

392   speaking, the condition of one of stress tensor principal axes being vertical is only satisfied if the

393   Earth's surface is considered as a free horizontal boundary with no traction. Not every stress state

394   has this property – principal axes may rotate in a vicinity of a major structural weakness.
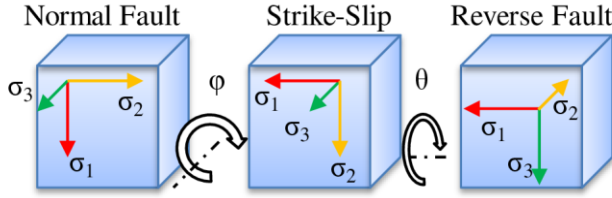
Figure 4. Schematic representation of transition between stress regimes with constant principal stresses magnitudes

Let's consider a hypothetical rotation of stress tensor principal axes using three Euler's angles. It is possible to change all Euler's angles simultaneously providing a complicated evolution of critically stressed fractures spatial orientations. The initial stress tensor σ_{ij}^0 has its maximum principal stress σ_1 directed vertically and intermediate stress σ_2 directed to the East – a typical Normal Fault stress regime. Initial stress state may be described as:

$$\sigma_{ij}^0 = \begin{bmatrix} \sigma_1 & 0 & 0 \\ 0 & \sigma_2 & 0 \\ 0 & 0 & \sigma_3 \end{bmatrix}, \tag{22}$$

in the proposed coordinate system (the first axis is vertical, the second is aimed at East; the third is aimed at North).

In the current paper Euler's angles are conventionally introduced to make it possible to transit from initial stress state (22) to the considered stress state (15). Principal stresses are the same for both stress states. Typical z-x-z convention is used here: the first Euler's angle φ stands for rotation of initial stress tensor about initial σ_3 direction (North); the second Euler's angle θ represents rotation about current σ_1 direction (rotations are consecutive); the third Euler's angle ψ stands for rotation about current σ_3 direction (Fig. 4). Note that $\varphi = \theta = \psi = 0$ represents pure Normal Fault regime; the first rotation leads to pure Strike-Slip regime when φ becomes equal to $\pi/2$; the second rotation results in pure Reverse Fault when θ becomes equal to $\pi/2$.

The final directions of principal stresses of stress tensor (15) – solution of equations 17 through may be calculated from the proposed Euler's angles as:

$$\begin{pmatrix} n_1^1 & n_2^1 & n_3^1 \\ n_1^2 & n_2^2 & n_3^2 \\ n_1^3 & n_2^3 & n_3^3 \end{pmatrix} = \begin{pmatrix} \cos\varphi\cos\psi - \cos\theta\sin\varphi\sin\psi & -\cos\psi\sin\varphi - \cos\varphi\cos\theta\sin\psi & \sin\theta\sin\psi \\ \cos\theta\cos\psi\sin\varphi + \cos\varphi\sin\psi & \cos\varphi\cos\theta\cos\psi - \sin\varphi\sin\psi & -\cos\psi\sin\theta \\ \sin\varphi\sin\theta & \cos\varphi\sin\theta & \cos\theta \end{pmatrix}. \tag{23}$$

417   If principal stresses magnitudes σ_1, σ_2, and σ_3 are fixed, variations φ, θ, $\psi \in (0; \pi)$ cover

418   all the possible stress states with these principal stresses. For example, stress state represented in

419   Fig. 3 may be analyzed from the perspective of Euler's angles as: $\varphi = 10^o$, $\theta = 15^o$, $\psi = 25^o$;

420   principal stresses ratio is: $\sigma_1/\sigma_2/\sigma_3 \approx 4/2/1$.

421   Figures 5 through 7 represent the described rotations of stress tensor and corresponding

422   changes in critically stressed fractures domain at the stereonet. A particular stress state with ratio

423     $\sigma_1/\sigma_2/\sigma_3$ being maintained as 4/2/1 was analyzed. Friction coefficient is set to 0.6.
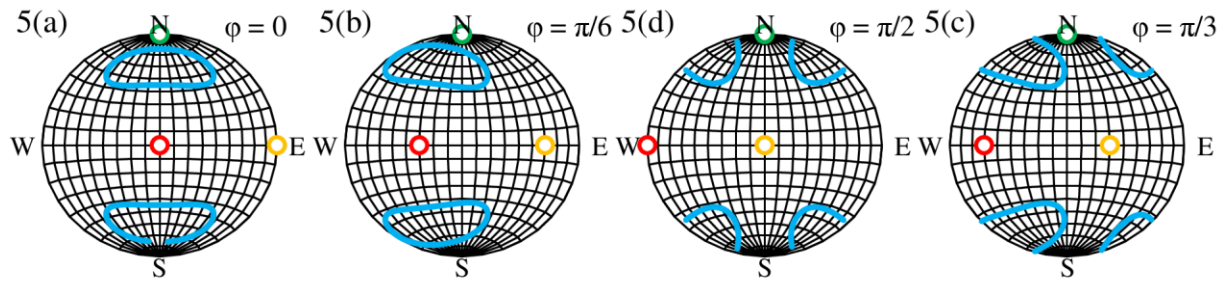

424

Figure 5. The first rotation about minimum principal stress direction ($\theta = \psi = 0$; φ is
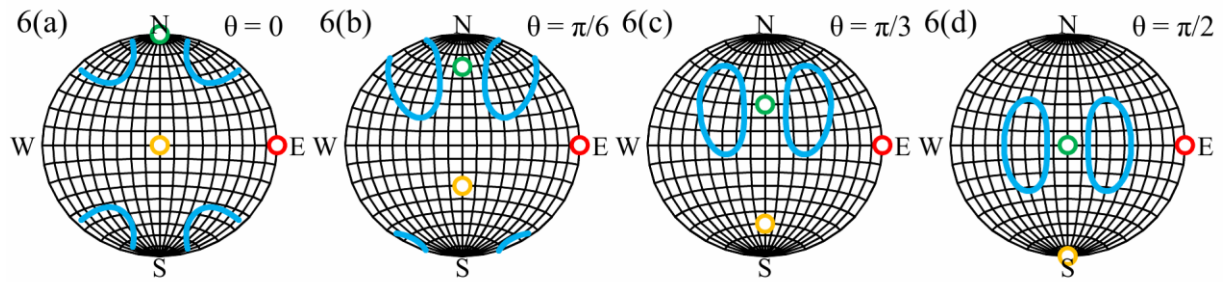
gradually increasing).

427

Figure 6. The second rotation about current maximum principal stress direction ($\varphi = \pi/2$,
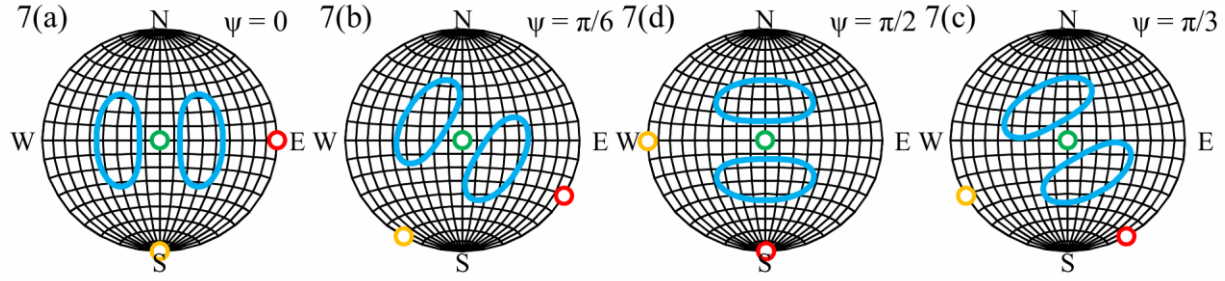
$\psi = 0$; θ is gradually increasing).

430

Figure 7. The third rotation about current minimum principal stress direction ($\varphi = \theta = \pi/2$; ψ is gradually increasing)

3.2 Transistional stress regimes

Previous section was devoted to rotation of principal axes of stress tensor with fixed values of principal stresses magnitudes. The next step is analysis of critically stressed fractures behavior under varied principal stresses magnitudes and fixed principal axes.

It is possible to study the relationship between principal stresses through stress tensor shape parameters proposed by Angelier (1979) and developed by Simpson (1997). Shape of any stress tensor may be quantitatively analyzed with the help of shape parameter ϕ that is closely related to Lode-Nadai coefficient:

$$\phi = (\sigma_2 - \sigma_3)/(\sigma_1 - \sigma_3). \tag{24}$$

This definition compares the magnitude of the intermediate stress σ_2 to the other principal stresses: if the intermediate stress is equal to minimum stress, ϕ approaches 0; if it is close to maximum stress, ϕ approaches 1.

There is no information regarding directions of principal axes in this definition, so this parameter was changed to improve its application in geomechanics: if one of the principal axes is aimed vertically, this parameter may be modified to include information about which particular stress is directed vertically. The following modified stress tensor shape parameter A_ϕ was introduced by Simpson (1997):

$$A_\phi = (s+0.5)+(-1)^s(\phi-0.5)=(s+0.5)+(-1)^s\left(\frac{\sigma_2-\sigma_3}{\sigma_1-\sigma_3}-0.5\right), \tag{25}$$

where s is an index number connected to the considered stress regime: $s = 0$ for normal stress regime (σ_1 is directed vertically, Fig. 5a); $s = 1$ for strike-slip (σ_2 is directed vertically,

453   Figures 5d and 6a); $s = 2$ for reverse fault (σ_3 is directed vertically, Fig. 7). A_ϕ ranges

454   continuously from 0 to 1 for normal, from 1 to 2 for strike-slip, and from 2 to 3 for reverse fault

455   stress regimes.

456   The proposed analytical solution to spatial orientations of critically stressed fractures

457   makes it possible to obtain these orientations for transitions between stress regimes caused by

458   gradual changes in stress tensor shape parameters.

459   Consider an initial stress tensor σ_{ij}^0 with principal stresses ratio $\sigma_1/\sigma_2/\sigma_3 = 4/1/1$; $\phi = 0$, A_ϕ

460    $= 0$, Normal Fault stress regime. Only principal stresses will be changed in this section, so

461   Euler's angles discussed in the previous section will be fixed. Critically stressed fractures has

462   been studied in an analogous way by Davidson et al. (2012) for a particular geothermal field with

463   maximum horizontal stress azimuth 56°, so the Euler's angles were chosen as $\varphi = 0^o$, $\theta = 56^o$, $\psi =$

464   0° to provide an opportunity to verify the obtained critically stressed fractures patterns. Once

465   again, all the procedures may be carried out for any combination of Euler's angles.

466   There are different opportunities to adjust stress tensor shape. Fig. 8 presents transition

467   between stress regimes caused by gradual increase of A_ϕ from 0 to 3 with fixed stresses σ_1 and

468   σ_3, under varied $\sigma_1 = \sigma_3 + A_\phi \cdot (\sigma_1 - \sigma_3)$. Isolines of different color are borderlines of domains of

469   critically stressed fractures for corresponding values of stress tensor shape coefficients. Fig. 8a

470   shows domains of critically stressed fractures for increasing A_ϕ for Normal Fault; Fig. 8b shows

471   domains of critically stressed fractures for increasing A_ϕ for Strike-Slip; Fig. 8c shows domains

472   of critically stressed fractures for increasing A_ϕ for Reverse Fault. Fig. 8b is analogous to the one

473   obtained by Davidson et al. (2012) (see Davidson et al. (2012), Fig. 8) and is in full quantitative
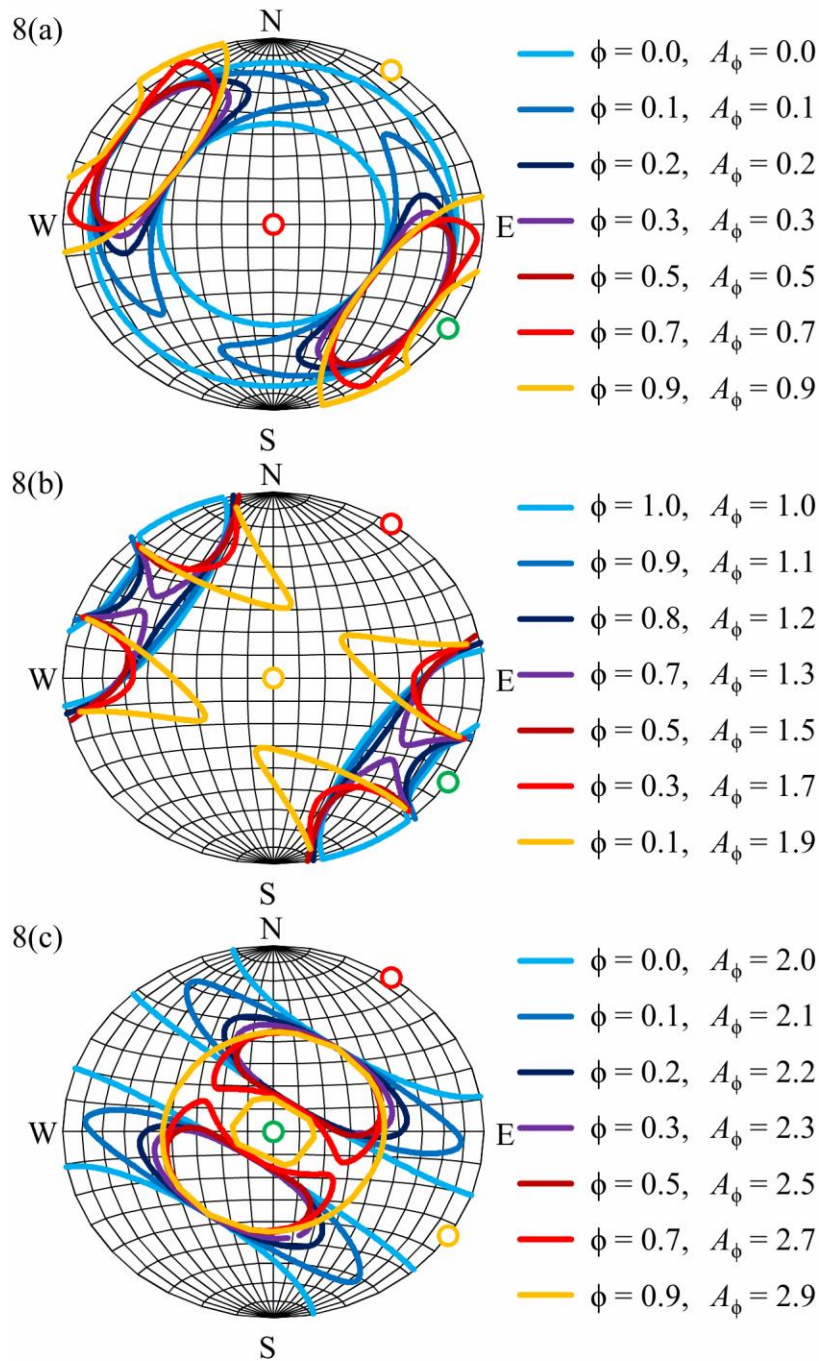
474   agreement with their results.

8(a)

—	$\phi = 0.0, \quad A_\phi = 0.0$
—	$\phi = 0.1, \quad A_\phi = 0.1$
—	$\phi = 0.2, \quad A_\phi = 0.2$
—	$\phi = 0.3, \quad A_\phi = 0.3$
—	$\phi = 0.5, \quad A_\phi = 0.5$
—	$\phi = 0.7, \quad A_\phi = 0.7$
—	$\phi = 0.9, \quad A_\phi = 0.9$

8(b)

—	$\phi = 1.0, \quad A_\phi = 1.0$
—	$\phi = 0.9, \quad A_\phi = 1.1$
—	$\phi = 0.8, \quad A_\phi = 1.2$
—	$\phi = 0.7, \quad A_\phi = 1.3$
—	$\phi = 0.5, \quad A_\phi = 1.5$
—	$\phi = 0.3, \quad A_\phi = 1.7$
—	$\phi = 0.1, \quad A_\phi = 1.9$

8(c)

—	$\phi = 0.0, \quad A_\phi = 2.0$
—	$\phi = 0.1, \quad A_\phi = 2.1$
—	$\phi = 0.2, \quad A_\phi = 2.2$
—	$\phi = 0.3, \quad A_\phi = 2.3$
—	$\phi = 0.5, \quad A_\phi = 2.5$
—	$\phi = 0.7, \quad A_\phi = 2.7$
—	$\phi = 0.9, \quad A_\phi = 2.9$

Figure 8. Transitions between stress regimes under fixed principal stresses directions and varied stress tensor shapes.

It can be clearly seen that the domains of critically stressed fractures are axis-symmetric for the cases of $A_\phi = 0, 1, 2$ which comes naturally from equations (1) through (3).

480   Critically stressed fractures domains show similar behavior under different ratios σ_1/σ_3.

481   As a result, variations of A_ϕ and σ_1/σ_3 ratios cover all possible principal stresses magnitudes.

482   These variations are summarized in Fig. 9 where relative amount of critically stressed fractures

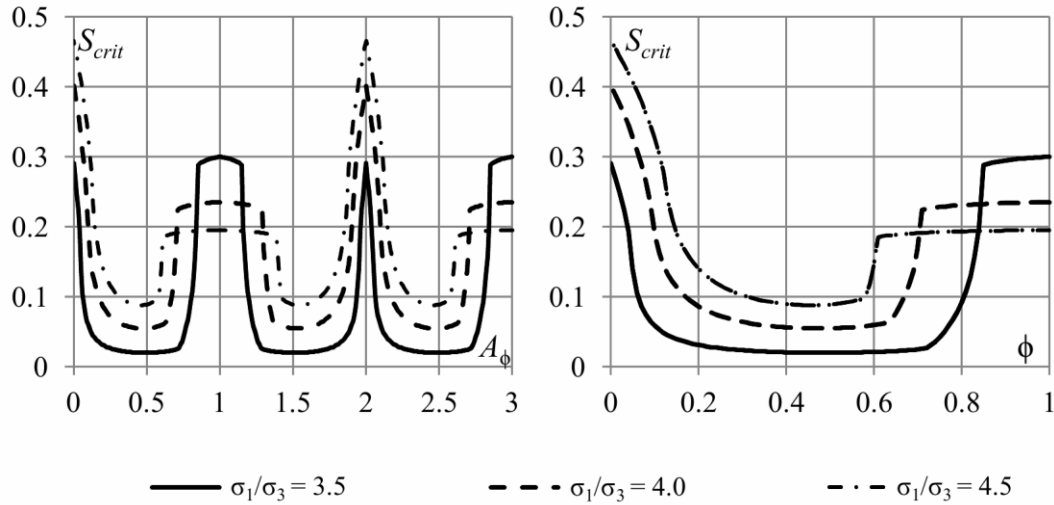483 S_{crit} introduced in equation (21) is plotted for different stress tensor shape parameters.

484

Figure 9. Relative amount of critically stressed fractures during transitions between stress
regimes under fixed principal stresses directions and varied stress tensor shapes.

487   Note that no critically fractures emerge if:

$$\frac{\sigma_1}{\sigma_3} \geq \frac{\sqrt{\mu^2+1}+\mu}{\sqrt{\mu^2+1}-\mu}, \tag{26}$$

489   following from equations (1) through (3). For the considered case of $\mu = 0.6$, minimum

490   ratio between maximum and minimum principal stress, providing an opportunity for critically

491   stressed fractures to emerge, is about 3.12. The maximum possible ratio between maximum and

492   minimum principal stresses is governed by rock strength properties. Fig. 9 represents evolution

493   of critically stressed fractures relative amount for a set of principal stresses ratios: $\sigma_1/\sigma_3 = 3.5$,

494   4.0, 4.5. As it can be clearly seen from equations (21), type of stress regime is not important for

495   relative amount of critically stressed fractures: only relationships between principal stresses

496   magnitudes matter. As a result, the same stress tensor shape parameter ϕ corresponding to

497   different generalized stress tensor shape parameters A_ϕ for different stress regimes provide the

498   same relative amont of critically stressed fractures. The following tendency is observed: relative

499   amount of critically stressed fractures is the greatest for $\phi = 0$ and 1, and the least in the middle

500   of transition with $\phi \approx 0.5$. The largest changes in relative amount of critically stressed fractures

501   appear when ϕ changes from 0 to 0.1 and when it exceeds 0.6.

502   **3.3 Denendency on friction coefficient**

503   Friction coefficient μ is the last parameter to analyze in the current study. All the

504   previous calculations were completed for a fixed friction coefficient $\mu = 0.6$. It is clear that an

505   increase in friction coefficient will lead to a corresponding decrease of domain of critically

506   stressed fractures.

507   Fig. 10 represents the evolution of critically stressed fractures domains at stereonets for a

508   set of typical fixed stress tensor shape parameters: $A_\phi = 0.3$; 0.7; 1.3; 1.7; 2.3; 2.7 covering all

509   transitional stress regimes. Color represents different values of friction coefficient $\mu = 0.4$; 0.5;

510   0.6; 0.7 with darker colors representing higher friction coefficients. It can be easily seen that an

511   increase in friction coefficient really leads to contraction of critically stressed fractures domain

512   with its center being close to spatial orientations of optimally oriented faults (Zoback, 2007).

513   This evolution is analyzed in the same way as in the previous section: Fig. 11 represents changes

514   in relative amount of critically stressed fractures obtained from equations 21 as a function of

515   friction coefficient for a fixed stress tensor shape parameter ϕ. Once again, same values of stress

516   tensor shape parameter ϕ obtained for different generalized stress tensor shape parameters A_ϕ (A_ϕ

517    $= \phi$ for Normal Fault; $A_\phi = 2 - \phi$ for Strike-Slip; $A_\phi = 2 + \phi$ for Reverse Fault) provide the same

518   relative amount of critically stressed fractures S_{crit} because stress regime is not considered in
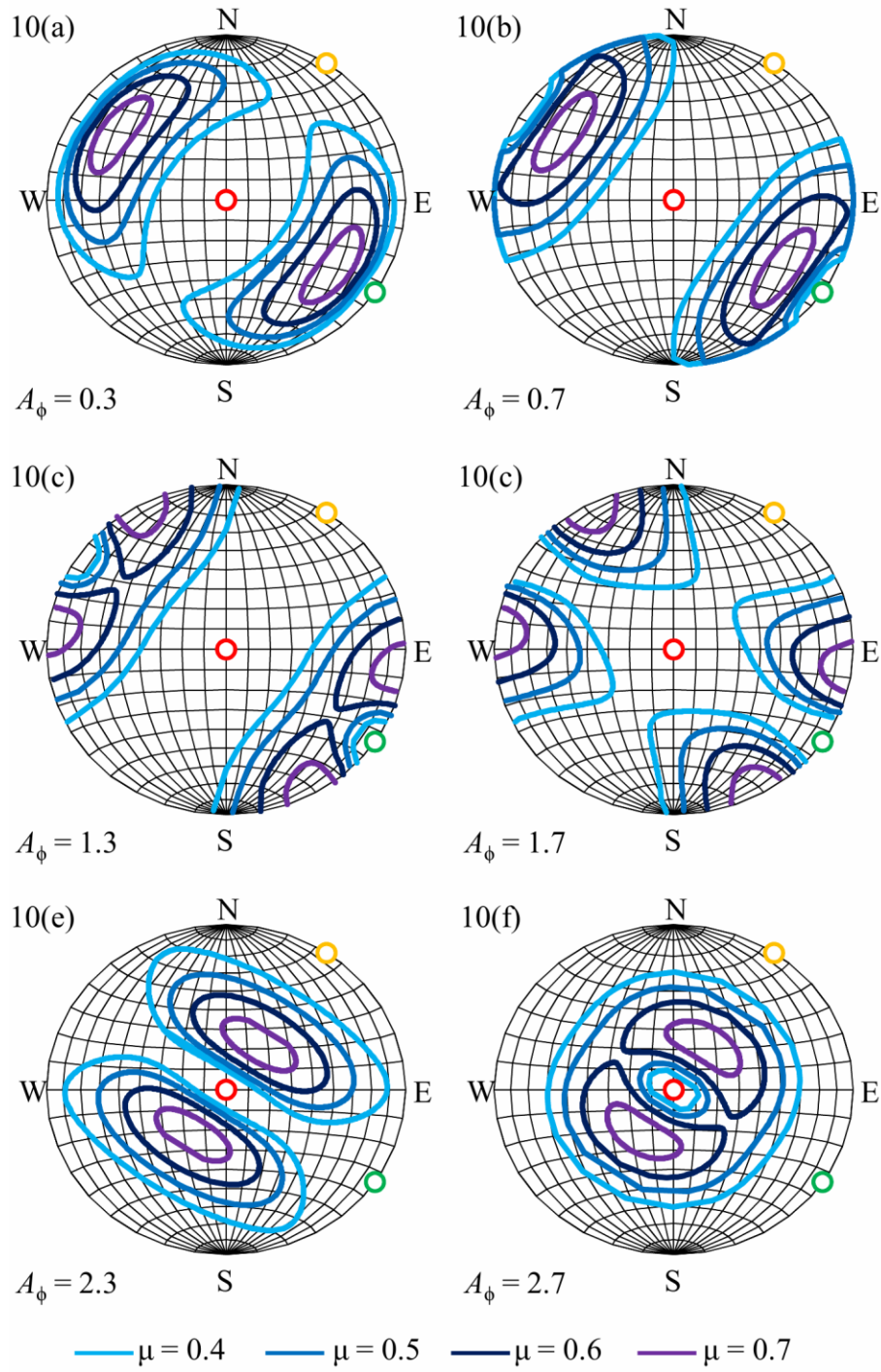
519   equations (21).

Figure 10. Critically stressed fractures domains for varied friction coefficient.
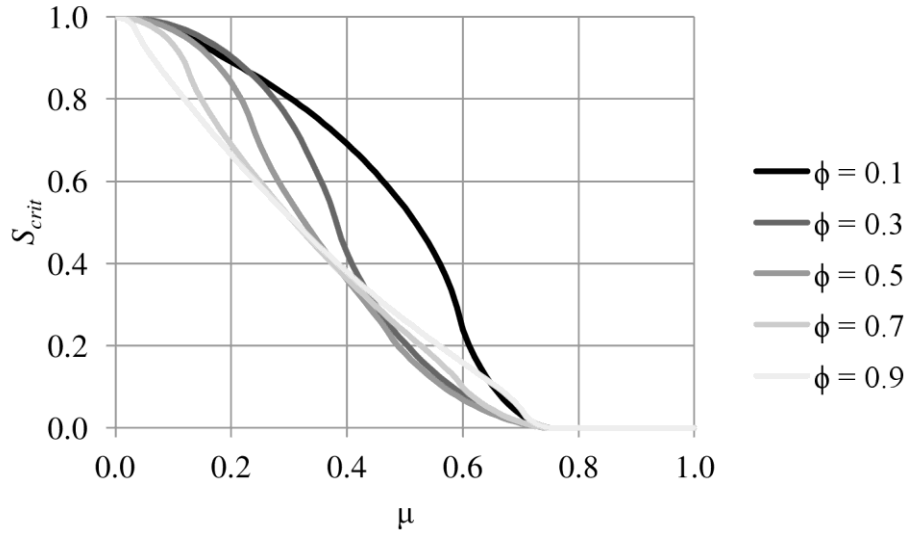
522

Figure 11. Relative amount of critically stressed fractures for varied friction coefficient

It is obvious from Fig. 11 that an increase in friction angle leads to a nonlinear decrease in relative amount of critically stressed fractures. Although Fig. 11 is plotted for a fixed principal stresses ratio $\sigma_1/\sigma_3 = 4/1$ and varied intermediate principal stress σ_2 (same as Fig. 8), this evolution is similar for other σ_1/σ_3 ratios: the plot moves to the right for the greater ratios. S_{crit} becomes zero once raw friction law becomes higher than Mohr circle. The possible values of friction coefficient μ corresponding to presence of critically stressed fractures may be directly calculated from equation (26):

$$\mu \leq \frac{\sigma_1/\sigma_3 - 1}{2\sqrt{\sigma_1/\sigma_3}}. \tag{27}$$

Magnitudes and directions of principal stresses alongside with friction coefficient of the rock are the only parameters influencing spatial orientations and relative amount S_{crit} of critically stressed fractures. In these sections each one of these parameters was analyzed from the perspective of critically stressed fractures spatial orientations and relative amount: Figures 5, 6, and 7 are focused on critically stressed fractures domains evolution caused by changes in principal stresses directions; Figures 8 and 9 are related to gradual changes of principal stresses magnitudes; and finally, Figures 10 and 11 deal with friction coefficient. As a result, any arbitrary stress tensor may be considered as combination of these three cases proving that the

540 proposed analytical solution is indeed suitable to understand critically stressed fractures patterns

541 for any geomechanical problem.

542 **4 Conclusions**

543   The obtained analytical solution makes it possible to calculate all possible spatial

544 orientations of critically stressed fractures for an arbitrary stress tensor acting in a fractured rock

545 mass with a known friction coefficient.

546   Taking into account numerous papers devoted to establishing the relationship between

547 critically stressed and hydraulically conductive fractures, knowledge of spatial orientations of

548 critically stressed fractures is an important step to understand the filtration paths in naturally

549 fractured rocks.

550   The proposed mathematical algorithm is strongly dependent on the input data – the

551 spatial distributions of stress tensor components. As far as these data are among the main results

552 of geomechanical modeling, which is frequently carried out at the current state of scientific and

553 engineering approaches to reservoir development, the proposed algorithm can be easily

554 integrated into existing solutions for geomechanical modeling. At the same time, such an

555 integration will increase the value of geomechanical modeling results without considerable

556 changes in costs as far as all the equations (6) through (16) are analytical.

557   According to the problem being solved during geomechanical modeling, one may use the

558 obtained analytical solution to consider specific processes in terms of critically stressed fractures.

559 The following problems of reservoir geomechanics may be particularly analyzed: forecast of

560 critically stressed fractures near a hydraulic fracture and creation of a branching network of

561 hydraulically conductive fractures through fluid injection; analysis of evolution of critically

562 stressed fractures' properties throughout reservoir development based on results of four-

563 dimensional geomechanical modeling and others; wellbore stability in fractured reservoirs and

564 other problems of reservoir geomechanics. It is also likely that there are other areas to apply the

565 obtained solution.

566   Spatial orientations of critically stressed fractures are the main focus of the current paper,

567 but there are also many important properties of the fractured medium not considered here. These

568 properties include sizes of the fractures, conductivity properties, shape and connectivity of the

569   fractures and others. Scaling factor was not considered in the current paper as well. The last

570   results of modeling the behavior of naturally fractured rock masses prove that these factors may

571   be taken into account if petroelastic modeling approaches are applied to predict effective

572   mechanical properties of fractured rock masses. It is worth to be highlighted that the analysis of

573   spatial orientations of critically stressed fractures should be completed beforehand leading to

574   increase in quality and reliability of input data for petroelastic modeling.

583   **References**

584   Allmendinger, R. W., Cardozo, N., & Fisher D. M. (2012). *Structural Geology Algorithms*

585   *Vectors and Tensors*. Cambridge: Cambridge University Press.

586   Anderson, E. M. (1951). The Dynamics of Faulting and Dyke Formation With Application to

587   Britain. Edinburgh: Oliver and Boyd.

588   Angelier, J. (1979). Determination of the mean principal stresses for a given fault population.

589   *Tectonophysics*, *56*(3–4), T17–T26. https://doi.org/10.1016/0040-1951(79)90081-7

590   Barton, C. A., Zoback, M. D., & Moos, D. (1995). Fluid flow along potentially active faults in

591   crystalline rocks. *Geology*, *23*(8), 683–686. https://doi.org/10.1130/0091-

592   7613(1995)023<0683:FFAPAF>2.3.CO;2

593   Bayuk, I. O., Dubinya, N. V., Garagash, I. A., Tikhotskiy, S. A., & Tikhotskaya, O. A. (2019).

594   *Multiscale Rock-Physics Modeling of Effective Elastic Properties of Fractured Reservoir Rocks.*

595   Paper presented at 53rd US Rock Mechanics/Geomechanics Symposium, American Rock

596   Mechanics Association, New York City, NY.

597   Biot, M. A. (1955). Theory of elasticity and consolidation for a porous anisotropic solid. *Journal*

598   *of Applied Physics*, *26*(2), 182–185. https://doi.org/10.1063/1.1721956

599   Bisdom, K., Bertotti, G., & Nick, H. M. (2016). The impact of different aperture distribution

600   models and critical stress criteria on equivalent permeability in fractured rocks. *Journal of*

601   *Geophysical Research: Solid Earth, 121*(5), 4045–4063. https://doi.org/10.1002/2015JB012657

602   Byerlee, J. (1978). Friction of Rocks. *Pure and Applied Geophysics*, *116*, 615–626.

603   https://doi.org/10.1007/BF00876528

604   Célérier, B. (1995). Tectonic regime and slip orientation of reactivated faults. *Geophysical*

605   *Journal International*, *121*(1), 143–161. https://doi.org/10.1111/j.1365-246X.1995.tb03517.x

606   Chan, A. W., Brem, A. G., & Abd Rahim, M. H. (2019). *Lost Circulations Due to Fault*

607   *Reactivation and the Implications on Stress Characterization*. Paper presented at 53rd US Rock

608   Mechanics/Geomechanics Symposium, American Rock Mechanics Association, New York City,

609   NY.

610   Coussy, O. (2004). *Poromechanics*. West Sussex: John Wiley & Sons Ltd.

611   Davatzes, N. C. & Hickman, S. H. (2010). *The Feedback Between Stress, Faulting, and Fluid*

612   *Flow: Lessons from the Coso Geothermal Field, CA, USA*. Paper presented at World Geothermal

613   Congress, International Geothermal Association, Bali, Indonesia.

614   Davidson, J., Siratovich, P., Wallis, I., Gravley, D., & McNamara, D. (2012). Quantifying the

615   stress distribution at the Rotokawa geothermal field, New Zealand. Paper presented at New

616   Zealand Geothermal Workshop, Auckland, New Zealand.

617   Dubinya, N. (2019). *Stress state estimation based on local variations of effective elastic moduli*

618   *caused by presence of critically stressed fractures*. Paper presented at 53rd US Rock

619   Mechanics/Geomechanics Symposium, American Rock Mechanics Association, New York City,

620   NY.

621   Dubinya, N. V., & Ezhov, K. (2017). A. In-situ horizontal stress estimation based on the

622   geometrical properties of fractures in well vicinity. *Geophysical Research*, 18(2), 5–26.

623   https://doi.org/10.21455/gr2017.2-1

624   Dubinya, N. V., & Fokin, I. V. (2018). *Nonlinear Model for Reversible Deformation of Rock*

625   *Containing Critically Stressed Fractures*. Paper presented at 52nd U.S. Rock

626   Mechanics/Geomechanics Symposium, American Association of Rock Mechanics, Seattle, WA.

627   Fisher, Q. J., Casey, M., Harris, S. D., & Knipe, R. J. (2003). Fluid-flow properties of faults in

628   sandstone: The importance of temperature history. *Geology*, *31*(11), 965–968.

629   https://doi.org/10.1130/G19823.1

630   Guiraud, M., Laborde, O., & Philip, H. (1989). Characterization of various types of deformation

631   and their corresponding deviatoric stress tensors using microfault analysis. *Tectonophysics*,

632   *170*(3-4), 289–316. https://doi.org/10.1016/0040-1951(89)90277-1

633   Hickman, S. H., Barton, C. A., Zoback, M. D., Morin. R., Sass, J., & Benoit, R. (1997). In situ

634   stress and fracture permeability along the Stillwater fault zone, Dixie Valley, Nevada.

635   *International Journal of Rock Mechanics and Mining Sciences & Geomechanics Abstracts*, *34*

636   (3–4), 414. https://doi.org/10.1016/S0148-9062(97)00169-1

637   Ito, T., Fujii, R., Evans, K. F., & Hayashi, K. (2002). Estimation of Stress Profile with Depth

638   from Analysis of Temperature and Fracture Orientation Logs in a 3.6 km Deep Well at Soultz,

639   France. Paper presented at SPE/ISRM Rock Mechanics Conference, Society of Petrolum

640   Engineers, Irwing, TX. https://doi.org/10.2118/78185-MS

641   Ito, T., & Zoback, M. D. (2000). Fracture permeability and in situ stress to 7 km depth in the

642   KTB scientific drillhole. *Geophysical Research Letters*, *27*(7), 1045–1048.

643   https://doi.org/10.1029/1999GL011068

644   Kolditz, O., Gorke, U. J., Shao. H., & Wang, W. (2016). *Thermo-Hydro-Mechanical-Chemical*

645   *Processes in Porous Media: Benchmarks and Examples.* Switzerland: Springer International

646   Publishing.

647   Ligtenberg, J. H. (2005). Detection of fluid migration pathways in seismic data: implications for

648   fault seal analysis. *Basin Research*, *17*, 141–153. https://doi.org/10.1111/j.1365-

649   2117.2005.00258.x

650 Massiot, C., Nicol, A., McNamara, D. D., & Townend, J. (2017). Evidence for tectonic,

651 lithologic, and thermal controls on fracture system geometries in andesitic high-temperature

652 geothermal field. *Journal of Geophysical Research: Solid Earth*, *122*(8), 6853–6874.

653 https://doi.org/10.1002/2017JB014121

654 Mattila, J. & Follin, S. (2019) Does In Situ State of Stress Affect Fracture Flow in Crystalline

655 Settings? *Journal of Geophysical Research: Solid Earth*, *124*(5), 5241–5253.

656 https://doi.org/10.1029/2018JB016791

657 Philip, H. (1987). Plio-Quaternary evolution of the stress field in Mediterranean zones of

658 subduction and collision. *Annales geophysicae. Series B. Terrestrial and planetary physics*, *5*(2),

659 301–319.

660 Rogers, S. (2003). Critical stress-related permeability in fractured rocks. Fracture and in situ

661 stress characterization of hydrocarbon reservoirs. *Geological Society, London, Special*

662 *Publications*, *209*(1), 7–16. https://doi.org/10.1144/GSL.SP.2003.209.01.02

663 Sathar, S., Reeves, H. J., Cuss, R. J., & Harrington, J. F. (2012). The role of stress history on the

664 flow of fluids through fractures. *Mineralogical Magazine*, *76*(8), 3165–3177.

665 https://doi.org/10.1180/minmag.2012.076.8.30

666 Schwab, D. R., Bidgoli, T. S., & Taylor, M. H. (2017). Characterizing the potential for injection-

667 induced fault reactivation through subsurface structural mapping and stress field analysis,

668 Wellington Field, Sumner County, Kansas. *Journal of Geophysical Research: Solid Earth*, *122*,

669 10,132–10,154. https://doi.org/10.1002/2017JB014071

670 Silva, I., Domingos, F., Marinho, P., Laronga, R., & Khan, S. (2003). *Advanced Borehole Image*

671 *Applications in Turbidite Reservoirs Drilled With Oil Based Mud: A Case Study From Deep*

672 *Offshore Angola*. Paper presented at SPWLA 44th Annual Logging Symposium, Society of

673 Petrophysicists and Well-Log Analysts, Galveston, TX.

674 Simpson, R. W. (1997). Quantifying Anderson's fault types. *Journal of Geophysical Research:*

675 *Solid Earth*, *102*(B8), 17,909–17,919. https://doi.org/10.1029/97JB01274

676 Snyder, J. P. (1987). *Map Projections – A Working Manual*. Washngton D.C.: U.S. Government

677 Printing Office.

678   Townend, J., Zoback, M. D. (2000). How faulting keeps the crust strong. *Geology*, *28*(5), 399–

679   402. https://doi.org/10.1130/0091-7613(2000)28<399:HFKTCS>2.0.CO;2

680   Zhu, H., Jin, X., Guo, J., An, F., Wang, Y., & Lai, X. (2016). Coupled flow, stress and damage

681   modelling of interactions between hydraulic fractures and natural fractures in shale gas

682   reservoirs. *International Journal of Oil, Gas and Coal Technology*, *13*(4), 359–390.

683   http://dx.doi.org/10.1504/IJOGCT.2016.080095

684   Zoback, M. D. (2007). *Reservoir Geomechanics*. Cambridge: Cambridge University Press.